

A method for modelling radar interferograms without phase unwrapping: application to the M 5 FawnSkin, California earthquake of 1992 December 4

Kurt L. Feigl and Clifford H. Thurber

Department of Geology and Geophysics, University of Wisconsin-Madison, 1215 West Dayton Street, Madison, WI 53706, USA. E-mail: feigl@wisc.edu

Accepted 2008 June 11. Received 2008 April 12; in original form 2007 July 13

SUMMARY

Interferometric analysis of synthetic aperture radar images (InSAR) measures the phase shifts between two images acquired at two distinct times. These ambiguous ‘wrapped’ phase values range from $-\frac{1}{2}$ to $+\frac{1}{2}$ cycles. The standard approach interprets the phase values in terms of the change in distance between the ground and the radar instrument by resolving the integer ambiguities in a process known as ‘unwrapping’. To avoid unwrapping, we have developed, validated and applied a new method for modelling the wrapped phase data directly. The method defines a cost function in terms of wrapped phase to measure the misfit between the observed and modelled values of phase. By minimizing the cost function with a simulated annealing algorithm, the method estimates parameters in a non-linear model. Since the wrapped phase residuals are compatible with a von Mises distribution, several parametric statistical tests can be used to evaluate the fit of the model to the data. The method, named General Inversion for Phase Technique (GIPhT), can handle noisy, wrapped phase data. Applying GIPhT to two interferograms in the area of FawnSkin, California, we estimate a set of model parameters describing a magnitude 5 aftershock of the 1992 Landers earthquake. The resulting simulation fits the data well. The phase final residuals have a circular mean deviation less than 0.15 cycles per datum. Sampling the final residuals, we find the circular standard deviation of a phase measurement to be approximately 0.2 cycle, corresponding to 6 mm in range.

Key words: Time series analysis; Image processing; Inverse theory; Radar interferometry; Satellite geodesy.

1 INTRODUCTION

Interferometric analysis of synthetic aperture radar images (InSAR) is a geodetic technique that calculates the interference pattern caused by the difference in phase between two images acquired by a space-borne SAR at two distinct times. The resulting interferogram is a contour map of the change in distance between the ground and the radar instrument. These maps provide an unsurpassed spatial sampling density (~ 100 pixels km^{-2}), a competitive precision (~ 10 mm) and a useful observation cadence (1 pass month $^{-1}$). This unique remote-sensing tool has been demonstrated and validated for many actively deforming areas, including natural earthquakes and anthropogenic activity, as reviewed by Massonnet & Feigl (1998). Each time a radar sensor acquires an image, it records, for each pixel, a complex number composed of an amplitude and a phase. The amplitude measures the backscatter or the intensity of electromagnetic radiation reflected by the ground back to the radar antenna. The phase provides a measurement of the round trip traveltimes (and thus the distance) between the satellite and the ground. Given two

such complex images acquired at two distinct times, InSAR can provide four data products: two amplitude images, a map of the phase shift (called an interferogram) and a map of the spatial coherence (the degree of resemblance in the phase shift between neighbouring pixels). All four of these maps are typically registered to a digital elevation model (DEM) in geographic or cartographic coordinates within ~ 10 m.

The InSAR phase values range from $-\frac{1}{2}$ to $+\frac{1}{2}$ cycles. They are ambiguous because they are determined only to within an unknown integer number of cycles. Accordingly, they are called ‘wrapped’ phase values. To interpret them in terms of range change in millimetres, however, the standard approach requires resolving the integer ambiguities in a process known as ‘unwrapping’. For example, the study described below (Feigl *et al.* 1995) used fringes that were counted, or ‘unwrapped’, by manually digitizing the coordinates of each of the four fringes, corresponding to 16, 44, 72 and 100 mm, respectively of range decrease, or motion towards the satellite. Sophisticated algorithms exist for unwrapping fringe maps automatically (e.g. Ghiglia *et al.* 1987, Ghiglia & Romero 1994;

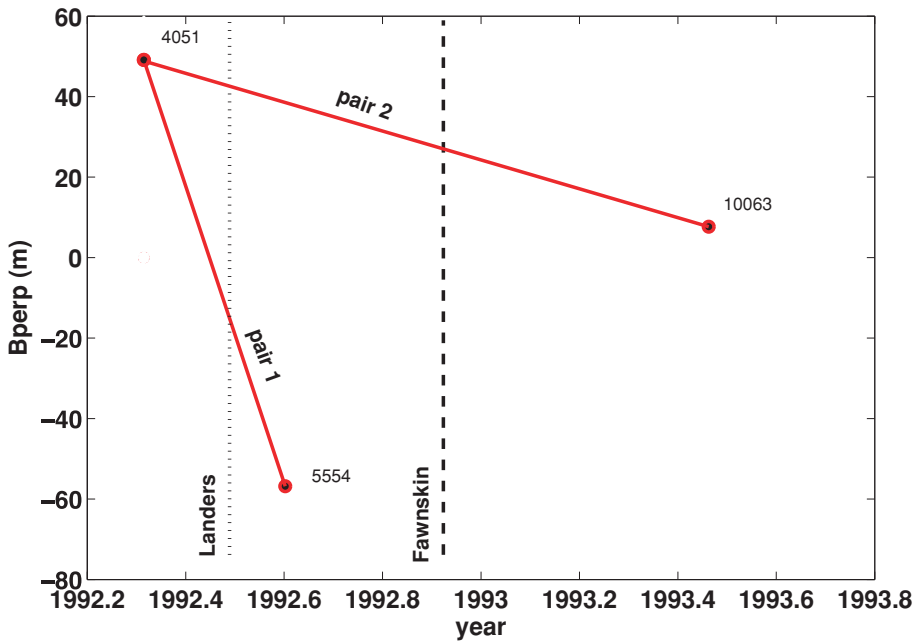


Figure 1. Orbital separation versus time for the radar images analysed in this study showing the three individual images (epochs) as circles. The two interferometric pairs are shown as line segments connecting the circles. The horizontal coordinate displays the acquisition date (epoch) of each image in decimal years. The labels next to the circles give the orbit numbers for the ERS-1 satellite. The vertical coordinate shows the orbital separation, or perpendicular component of the ‘baseline’ vector between the positions of the radar sensor at the acquisition epoch. The dotted line shows the date of the M 7.3 Landers main shock on 1992 June 28. The dashed line shows the date of the M 5.3 Fawn skin aftershock on 1992 December 4.

Zebker *et al.* 1994; Marroquin & Rivera 1995; Ghiglia 1998; Chen & Zebker 2000, 2001, 2002). Many InSAR studies use unwrapped phase data (e.g. Wright *et al.* 1999, 2001; Mellors *et al.* 2004; Talebian *et al.* 2004; Biggs *et al.* 2006). Unwrapping has three potential drawbacks for pre-processing the data before using them to estimate source parameters in an inversion. First, these algorithms can break down in areas where the phase is noisy as a result of decorrelation, possibly missing part of the signal. For example, a branch-cut algorithm (Goldstein *et al.* 1988) could unwrap only 44 of 77 interseismic interferograms crossing the Denali Fault (Biggs *et al.* 2007). Second, unwrapping algorithms can incorrectly estimate the integer part of the phase count, missing a ‘cycle slip’, especially if the coseismic rupture at the earth’s surface creates discontinuities in the fringe pattern. In this case, the error can be large, at least 28 mm in range, which is four times larger than the root mean square scatter in the range residuals for a typical InSAR study (Feigl *et al.* 1995). Although such unwrapping errors can be identified by phase misclosure over a loop of pairs, this approach is “difficult to implement automatically and time-consuming to implement manually...so that even the ‘corrected’ data set contains a large number of small unwrapping errors” (Biggs *et al.* 2007). Third, many unwrapping algorithms do not provide an estimate of uncertainty for their output unwrapped phase values, hindering the calculation of uncertainties for parameters estimated from them.

To work around these issues, we have developed, validated and applied a new method to model the phase data directly, without unwrapping. The new idea here is to assess the misfit between model and data with a cost function defined in terms of wrapped phase. By minimizing the cost function with a simulated annealing algorithm (Kirkpatrick *et al.* 1983), we can solve simultaneously for both linear and non-linear parameters. We call this method the General Inversion for Phase Technique (GIPhT).

2 IN SAR OBSERVATIONS OF THE FAWSKIN EARTHQUAKE

To validate our method, we apply GIPhT to interferograms covering the epicentral area of a magnitude 5 earthquake in California on 1992 December 4. This event occurred at 02:08 GMT near the town of Fawn skin on Big Bear Lake (Hauksson *et al.* 1993; Jones & Hough 1994). Unlike most of the other Landers aftershocks with local magnitude M_L of 5 or greater, it has a thrust mechanism (Hauksson *et al.* 1993; Jones & Hough 1994). Such a mechanism creates predominantly vertical displacements at the surface, which are more readily detected by radar than horizontal displacements. This sensitivity is a geometric consequence of the 23° angle of incidence used by the ERS-1 radar. Similarly, the shallow hypocentral depth of 2 km estimated from the seismological data (Hauksson *et al.* 1993) creates larger displacements at the surface than deeper events of the same magnitude.

The area around the epicentre was mapped by InSAR in a data set that includes two interferograms that have been published previously (Massonnet *et al.* 1993, 1994). The two interferograms span different intervals of time, as shown in Fig. 1. The first interferogram spans the 1992.3–1992.6 time interval (Fig. 2a). It shows the coseismic deformation produced by the Landers main shock at epoch 1992.6 as two sets of parallel fringes trending from northwest to southeast. This interferogram does not show the effects of the Fawn skin aftershock because that earthquake occurred at epoch 1992.9 after the acquisition date of the second image in the interferometric pair. The second interferogram spans the 1992.3–1993.5 time interval, including both the Landers main shock and the Fawn skin aftershock (Fig. 3a). As described previously (Feigl *et al.* 1995), the fundamental observation in the second interferogram consists of several rounded fringes centred on a point less than 2 km from the epicentral

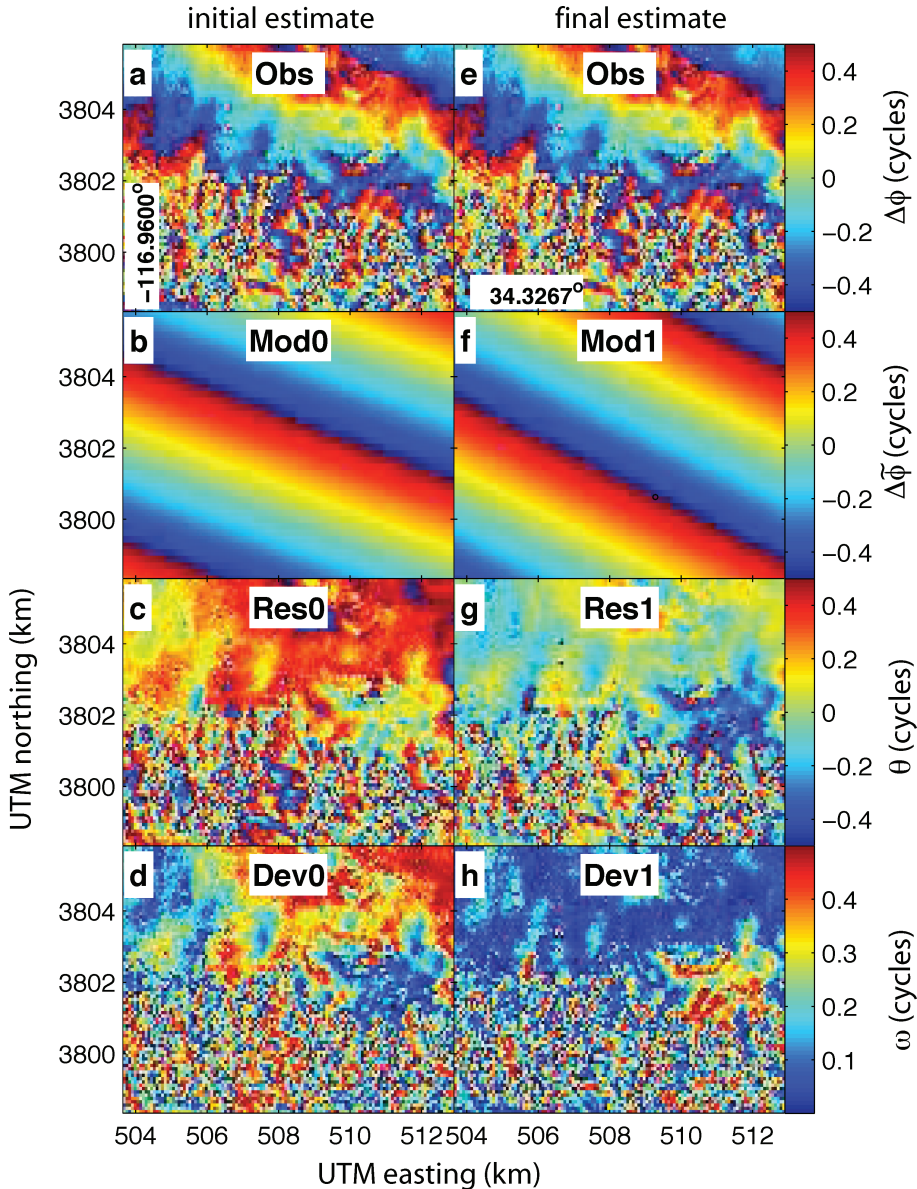


Figure 2. Interferograms for pair 1 spanning the 1992.3–1992.6 time interval that includes only the Landers main shock at epoch 1992.5, showing parallel fringes produced by coseismic deformation during that earthquake. The panels include (a) observed phase values $\Delta\phi_i$; (b) modelled phase values $\tilde{\phi}_i^{(initial)}$ calculated from the initial estimate; (c) initial residual phase values $\theta_i^{(initial)}$ formed by subtracting the initial modelled phase values from the observed phase values; (d) angular deviations $\omega_i^{(initial)}$ for the initial estimate; (e) observed phase values $\Delta\phi_i$, repeated for convenience; (f) modelled phase values $\tilde{\phi}_i^{(final)}$ calculated from the final estimate; (g) final residual phase values $\theta_i^{(final)}$ formed by subtracting the final modelled values from the observed phase values; and (h) angular deviations $\omega_i^{(final)}$ for the final estimate. In the upper three rows, one coloured fringe corresponds to one cycle of phase change, or 28 mm of range change. In the lowermost (fourth) row, the colours denote the angular deviation ω in phase between 0 and $\frac{1}{2}$ cycle. Coordinates are Universal Transverse Mercator easting and northing in km outside the frames; latitude and longitude in degrees inside.

location estimated from regional seismograms (Hauksson *et al.* 1993). After identifying the event as an earthquake by the ‘pairwise logic of discrimination’ (Massonnet & Feigl 1995), Feigl *et al.* (1995) estimated its location, depth, focal mechanism, slip vector, length and width. The model parameters were estimated from the unwrapped fringe changes in the second interferogram using an iterative least-squares algorithm to solve the non-linear inverse problem. The formal uncertainties of the estimated position of the centroid are less than 300 m in all three components. These uncertainties are smaller than the difference between two seismological estimates of the hypocentral location, and are also smaller than the dimensions of the fault area that ruptured. In this study, we esti-

mate the parameters directly from the wrapped phase data in both interferograms using a simulated annealing algorithm.

3 FORMALISM FOR A FORWARD MODEL

For a single pixel in an interferometric pair, we write the phase change between the first image acquired at time epoch t_1 and a second image acquired at a later time epoch t_2 as

$$\Delta\phi = \phi(t_2) - \phi(t_1). \quad (1)$$

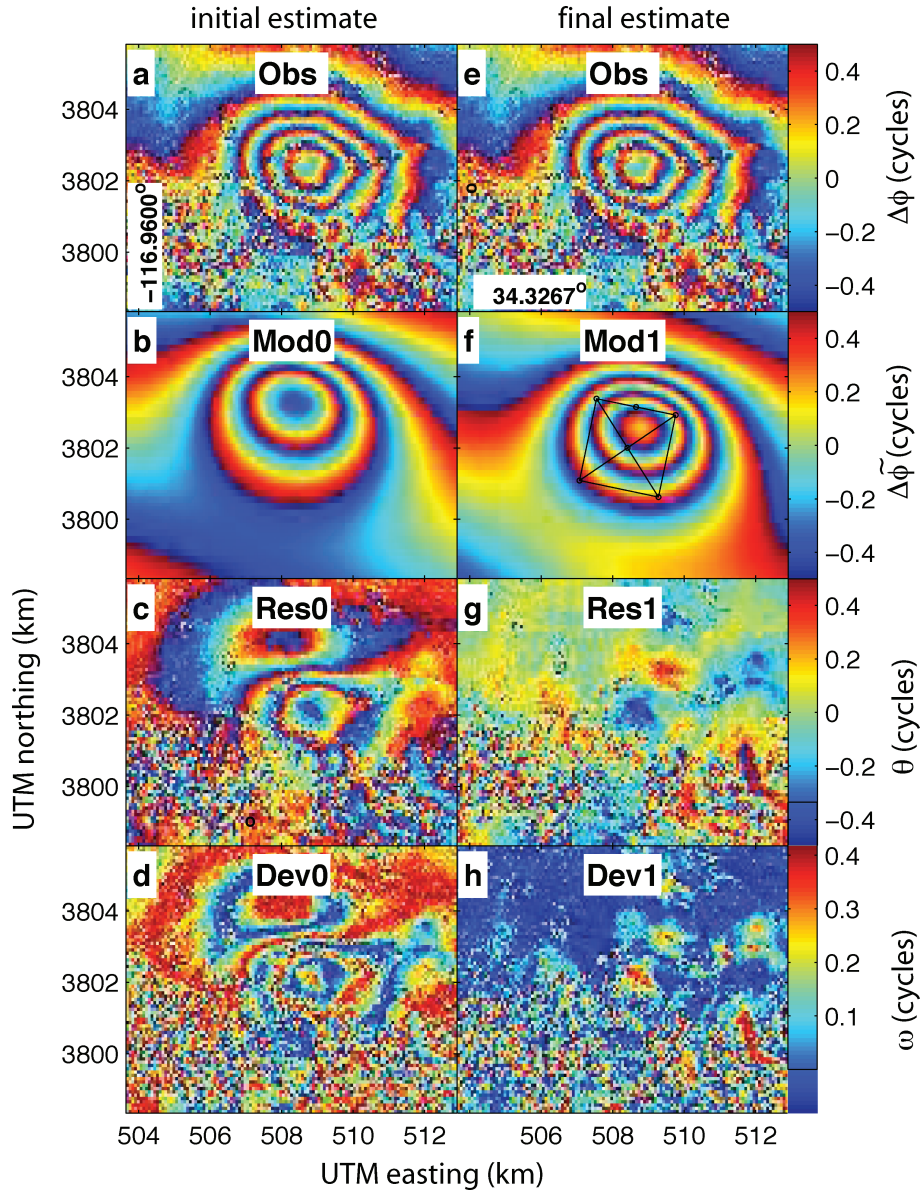


Figure 3. Interferograms for pair 2 spanning the 1992.3–1993.5 time interval that includes both the Landers main shock and the FawnSkin aftershock, showing that the final estimate (right-hand column) fits the data better than does the initial estimate (left-hand column). Panels and plotting conventions as in previous figure. In panel (f), the black rectangle shows the corners of the south-dipping fault patch that slipped during the FawnSkin earthquake at epoch 1992.9 calculated from the final estimate.

Generalizing to a time-series of images, with $q \geq 2$ epochs forming $c \geq 1$ pairwise combinations, we write the vector of phase changes for the k th pixel as the product of a matrix and a column vector

$$\Delta\phi_i^{(k)} = D_{ij}^{(k)}\phi^{(k)}(t_j), \quad (2)$$

where $D_{ij}^{(k)}$ is a differencing matrix defined so that its element at row i and column j equals -1 when epoch t_j is first, $+1$ when epoch t_j is second and 0 elsewhere. The row index i ranges over the c pairs and the column index j ranges over the q epochs. Repetition of the pixel index k does not imply summation here or anywhere else in this paper. Thus the differencing matrix $D_{ij}^{(k)}$ for pixel k has c rows and q columns.

The system of equations described by (2) thus specifies the phase change at the location of the k th pixel during the i th time interval. As written in (2), the phase change is a function of time (indices i

and j range over epochs) and position (index k ranges over pixels). The order of the pixels assigned by the index k is arbitrary. In other words, we do not assume any particular spatial structure for the 2-D arrays of pixels. For simplicity, however, we will assume that the positional dependence and temporal dependence are separable, as suggested by Fialko (2004). Accordingly, we write the modelled phase value for a single pixel with index k at a single epoch t_i as

$$\tilde{\phi}^{(k)}(t_i) = f(t_i)g^{(k)} + h_i^{(k)}, \quad (3)$$

where f is a function of time only; g is a mapping function of position only that describes the signal of interest, the geophysical deformation on the ground; and each h_i is a mapping function of position only that describes the nuisance effects pertaining to a single epoch, such as tropospheric perturbations or errors in the satellite's orbital trajectory. The modelled value of the change in phase for a single pixel with index k over the time interval from t_i

to t_j is

$$\Delta\tilde{\phi}[t_i, t_j, \mathbf{X}^{(k)}] = [f(t_j) - f(t_i)]g^{(k)} + h_j^{(k)} - h_i^{(k)}. \quad (4)$$

The time dependence of the geophysical deformation is described by the scalar function $f(t)$. In the case of a coseismic deformation field produced by an earthquake at time epoch t_s , we have $f(t) = H(t_s)$ where H is the Heaviside step function.

The positional dependence is described by the mapping function $g^{(k)} = g[\mathbf{X}^{(k)}]$ as a function of the position coordinate of the k th pixel $\mathbf{X}^{(k)} = [X_E^{(k)} X_N^{(k)} X_U^{(k)}]$ written as easting, northing and upward components reckoned in a local Cartesian reference system. The shape of the deformation field in map view is $g^{(k)} = -\mathbf{u} \cdot \hat{\mathbf{s}}$ where \mathbf{u} is the vector field of coseismic displacements at the surface of the Earth and $\hat{\mathbf{s}}$ is a unit vector pointing from the pixel on the ground to the radar sensor along the line of sight. The minus sign renders purely downward displacement ($u_U < 0$) a positive increase in range as the ground moves away from the satellite. The coseismic displacement field \mathbf{u} may be approximated as that due to a dislocation buried in a uniform, isotropic and elastic half-space (Okada 1985). The set of model parameters \mathbf{m} of interest are thus the earthquake source parameters describing the fault rupture, for example, slip, length, width, strike, dip and rake (e.g. Feigl 2002). Thus the mapping function describing the coseismic deformation field is

$$g^{(k)} = -[u_E^{(k)}(\mathbf{m}) u_N^{(k)}(\mathbf{m}) u_U^{(k)}(\mathbf{m})] \begin{bmatrix} \hat{s}_E^{(k)} \\ \hat{s}_N^{(k)} \\ \hat{s}_U^{(k)} \end{bmatrix}, \quad (5)$$

where the subscripts E , N and U denote the east, north and upward components, respectively, of the displacement vector \mathbf{u} and of the unit vector $\hat{\mathbf{s}}$.

Each of the nuisance functions $h_i^{(k)}$ depend on position (pixel index k). GIPhT allows one such function for each time epoch t_i . One simple parameterization is to consider a phase ramp (linear gradient) in each of the easting, northing and upward directions, respectively, at each epoch t_i

$$h_i^{(k)} = h_0(t_i) - \left[\begin{bmatrix} X_E^{(k)} - X_E^{(0)} \\ X_N^{(k)} - X_N^{(0)} \\ X_U^{(k)} - X_U^{(0)} \end{bmatrix} \right] h_E(t_i), \quad \left[\begin{bmatrix} X_E^{(k)} - X_E^{(0)} \\ X_N^{(k)} - X_N^{(0)} \\ X_U^{(k)} - X_U^{(0)} \end{bmatrix} \right] h_N(t_i), \\ \left[\begin{bmatrix} \hat{s}_E^{(k)} \\ \hat{s}_N^{(k)} \\ \hat{s}_U^{(k)} \end{bmatrix} \right], \quad (6)$$

where $\mathbf{X}^{(0)} = [X_E^{(0)} X_N^{(0)} X_U^{(0)}]$ denotes the position coordinates of the reference pixel with index $k = 0$. The first term accounts for the effect of the atmosphere and errors in the satellite's orbital trajectory. The upward vertical component h_U of the phase gradient accounts for the change in refractive index of the atmosphere with elevation. Its value can be as large as $h_U \doteq 3 \times 10^{-5}$, or approximately one C-band fringe per kilometre of topographic relief. It can vary over spatial scales as short as a few kilometres (e.g. Hanssen 2001). The horizontal components h_E and h_N of the phase gradient describe the fringe pattern contributed by errors in the satellite's orbital trajectory. Although the planar approximation is valid for small areas less than ~ 10 km in width, larger areas would require a description in terms of Keplerian orbital parameters (Kohlhase *et al.* 2003).

Other types of geophysical deformation could also be described using the same separable formulation. To describe secular motion on a locked fault, we would use the same mapping function $g^{(k)}$ but write the time dependence as $f(t) = t - t_0$ where t_0 is a reference

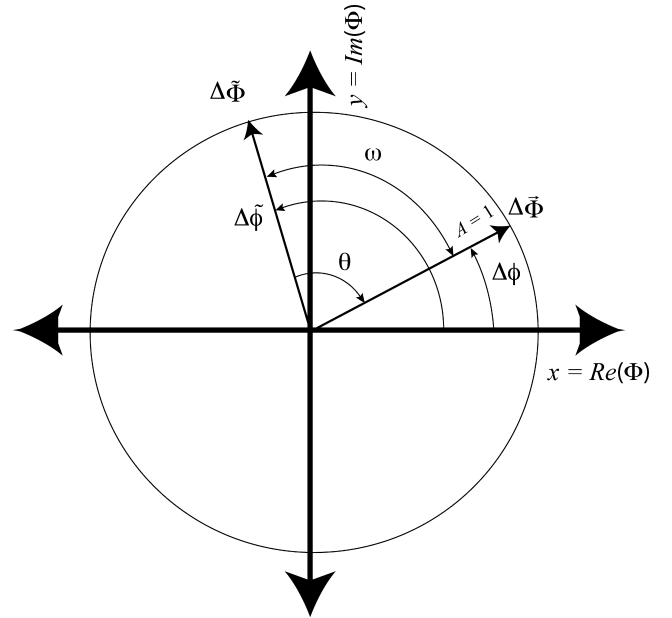


Figure 4. Sketch showing the observed phasor $\Delta\tilde{\Phi}$ and the modelled phasor $\Delta\Phi$, each with unit magnitude. The residual phase θ is the (signed) angular difference between the arguments of the two phasors, reckoned positive counter-clockwise. The angular deviation ω is the smallest (unsigned) angle between them. In this example: the observed value of the phase change $\Delta\phi = 0.1$ cycle, the modelled value of the phase change $\tilde{\Delta}\phi = 0.3$ cycle, the wrapped residual $\theta = -0.2$ cycle and the angular deviation between the observed and modelled values $\omega = 0.2$ cycle.

epoch. Similarly, post-seismic deformation following an earthquake at time epoch t_s might follow

$$f(t) = \{1 + \log[(t - t_s)/\tau]\}H(t_s), \quad (7)$$

where τ is a characteristic relaxation time (e.g. Feigl & Thatcher 2006). To describe periodic inflation and deflation, for example, seasonal subsidence, we could use Mogi's (1958) formulation for an infinitesimal spherical source in an elastic half-space for the mapping function $g^{(k)}$, but write the time dependence as

$$f(t) = \sin\left[\frac{2\pi(t - t_0)}{T}\right], \quad (8)$$

where T denotes the period, for example, 1 year for an annual signature.

4 SOLUTION

Given a measurement of phase change $\Delta\phi$ in cycles, we write it as a phasor with unit length (amplitude), as sketched in Fig. 4

$$\Delta\tilde{\Phi} = \begin{bmatrix} \cos(\Delta\phi) \\ \sin(\Delta\phi) \end{bmatrix}, \quad (9)$$

where the upper-case trigonometric functions have been adapted for an angular argument in cycles such that $\text{Sin}(\varphi) = \sin(2\pi\varphi)$ and $\text{Cos}(\varphi) = \cos(2\pi\varphi)$. The modelled value of the phasor is

$$\Delta\tilde{\Phi} = \begin{bmatrix} \cos(\Delta\tilde{\phi}) \\ \sin(\Delta\tilde{\phi}) \end{bmatrix}, \quad (10)$$

where the modelled value of the phase change $\Delta\tilde{\phi}$ is a function of the unknown parameters \mathbf{m} , as described in eq. (4). The wrapped

residual value of the phase change (in cycles) is

$$\theta = \text{wrap}(\Delta\phi - \Delta\tilde{\phi}), \quad (11)$$

where the wrapping operator can be calculated in several different ways, as discussed in the next paragraph. By definition, the wrapped phase residual θ varies between $-\frac{1}{2}$ and $+\frac{1}{2}$ cycle. In this respect, the wrap function differs from the modulus (1 cycle) operator because the latter returns a value between 0 and +1 cycle. Although the observed phase value is wrapped such that $-1/2 \leq \Delta\phi \leq +1/2$, the modelled phase value $\Delta\tilde{\phi}$ in (11) may be unwrapped such that $-\infty < \Delta\tilde{\phi} < \infty$.

To calculate the wrapped phase residual θ , we write

$$\theta = \frac{1}{2\pi} \text{ATAN2}\{\text{[Sin}(\Delta\phi - \Delta\tilde{\phi})], \text{[Cos}(\Delta\phi - \Delta\tilde{\phi})]\}\}, \quad (12)$$

where the $\text{ATAN2}(y, x)$ function in FORTRAN returns the angle (in radians) between the positive X -axis and the phasor formed by (x, y) in the trigonometric convention, i.e. reckoned positive counter-clockwise (Snyder 1982). Equivalently, in the MatlabTM programming language (MathWorks 2007), the wrapped residual phase is

$$\theta = \frac{1}{2\pi} \text{angle}\{\text{complex}\{\text{[Sin}(\Delta\phi - \Delta\tilde{\phi})], \text{[Cos}(\Delta\phi - \Delta\tilde{\phi})]\]\}\}. \quad (13)$$

The wrapped phase residual can also be calculated numerically using integer variables in a computer program to perform ‘subtraction without carry’ (Massonnet 1997).

Since the wrap function is not linear, standard least-squares algorithms do not apply to wrapped phase data. To avoid this issue, we define the angular deviation ω as the angle between the data phasor and the model phasor, as sketched in Fig. 4

$$\omega = \text{Cos}^{-1}(\Delta\vec{\Phi} \bullet \Delta\tilde{\Phi}), \quad (14)$$

where the dot indicates the inner (scalar) product and the inverse cosine function Cos^{-1} returns a non-negative value $0 \leq \omega < \frac{1}{2}$ cycle. For one data point, corresponding to the phase change in one pixel between two epochs, the angular deviation ω gives the smaller of the two angles between the data phasor $\Delta\vec{\Phi}$ and model phasor $\Delta\tilde{\Phi}$

$$\omega = \min[(\Delta\phi - \Delta\tilde{\phi}), 1 - (\Delta\phi - \Delta\tilde{\phi})], \quad (15)$$

where $\Delta\phi$ and $\Delta\tilde{\phi}$ are the observed and modelled values of the phase change, respectively. The same angle can also be calculated using the arc function as defined by Mardia (1972 p. 21) and named by Nikolaidis & Pitas (1998)

$$\omega = \text{arc}(\Delta\phi, \Delta\tilde{\phi}) = \frac{1}{2} - \left| \frac{1}{2} - |\Delta\phi - \Delta\tilde{\phi}| \right|. \quad (16)$$

The three expressions for the angular deviation ω are equivalent.

Since a large value of the angular deviation ω corresponds to a large misfit between the observed and modelled phase values, we define a cost function

$$\bar{\omega} = \frac{1}{n} \sum_{i=1}^n \omega_i, \quad (17)$$

where n is the number of data points. The cost function $\bar{\omega}$ may be interpreted geometrically as the mean of the L_1 norm of the angular deviations ω_i . It is equivalent to the circular mean deviation (Mardia 1972 p. 22) of the wrapped phase residuals θ_i

$$\bar{\omega} = \frac{1}{n} \sum_{i=1}^n [\text{arc}(\theta_i, \bar{\theta})] \quad (18)$$

if their mean direction $\bar{\theta} = 0$. In other words, the cost function $\bar{\omega}$ is equivalent to the mean of the L_1 norm of the wrapped residual phase values θ_i if their mean direction $\bar{\theta}$ is negligible. The cost $\bar{\omega}$ ranges from 0 to $\frac{1}{2}$ cycle. To find the optimal values of the parameters \mathbf{m} in the model, we minimize the cost function $\bar{\omega}$.

4.1 Comparison to previous approaches

Vadon & Sigmundsson (1997) solve the same problem by maximizing a score equal to the length of the sum of the residual phasors, that is, the pixel-by-pixel differences between the data and modelled phasors, normalized by the number of data points n

$$\frac{1}{n} \left\| \sum_{i=1}^n \{\Delta\vec{\Phi} - \Delta\tilde{\Phi}\}_i \right\|. \quad (19)$$

This quantity is called the ‘mean resultant length’ and denoted \bar{R} (Mardia 1972, p. 22)

$$\bar{R} = \sqrt{\bar{C}^2 + \bar{S}^2}, \quad (20)$$

where

$$\bar{C} = \frac{1}{n} \sum_{i=1}^n \text{Cos}(\Delta\phi_i - \Delta\tilde{\phi}_i) \quad (21)$$

and

$$\bar{S} = \frac{1}{n} \sum_{i=1}^n \text{Sin}(\Delta\phi_i - \Delta\tilde{\phi}_i). \quad (22)$$

Our scheme resembles that of Vadon & Sigmundsson (1997) because both our cost $\bar{\omega}$ and their score \bar{R} depend only on the wrapped phase values between $-\frac{1}{2}$ and $+\frac{1}{2}$ cycle. While we minimize the circular mean deviation $\bar{\omega}$, they maximize the mean resultant length \bar{R} . Although similar, these two statistics measure slightly different properties of the sample. The circular mean deviation $\bar{\omega}$ measures the dispersion about a mean direction that we assume to be zero. We test this assumption in Section 5.1, below. Calculating the mean resultant length \bar{R} , however, requires no such assumption. Accordingly, it admits the possibility of a systematic error in the modelled phase values, that is, the wrapped phase residuals concentrate about some mean direction other than zero. Since the circular mean deviation has the same units as the phase data, it also seems more physically intuitive than the mean resultant length \bar{R} . On the other hand, the mean resultant length \bar{R} is mathematically more convenient than the circular mean deviation for statistical analysis of directional data (Fisher 1993; Mardia & Jupp 2000).

Recently, an approach similar to the one suggested by Vadon & Sigmundsson (1997) has been applied to time-series of interferograms including many ($q \gtrsim 40$) epochs (Ferretti *et al.* 2000; Ferretti *et al.* 2001; Colesanti *et al.* 2003). As in the approach described by Vadon & Sigmundsson, the one described in these three studies considers the sum of the residual phasors, a quantity they call ‘multi-image, single-target coherence’ and write as γ (Colesanti *et al.* 2003). The expression for the absolute value of coherence $\|\gamma\|$ (eq. 5 in Colesanti *et al.* 2003) reduces to the mean resultant length \bar{R} , implying that $\|\gamma\| = \bar{R}$. Thus the two measures of goodness of fit are equivalent. In both cases, the measure is a value to be maximized. In the optimal case, where the model phase values perfectly match the observed data phase values, one has scores of $\bar{R} = \|\gamma\| = 1$ and a cost of $\bar{\omega} = 0$. In the worst case, when all the modelled phase values differ by exactly half a cycle from the observed phase values, one has scores of $\bar{R} = \|\gamma\| = 0$ and a cost

$\bar{\omega} = 1/2$ cycle. To solve the optimization problem, Vadon & Sigmundsson maximize \bar{R} by trial and error, whereas Colesanti *et al.* (2003) maximize $\|\gamma\|$ using non-parametric spectral estimation based on periodograms (Marple 1987). The statistical properties of the coherence operator γ have been described by Colesanti *et al.* (2003).

4.2 Solving the inverse problem

The inverse problem consists of estimating the model parameters \mathbf{m} from the phase data $\Delta\phi_i$. In the case where the phase data on the left-hand side of (2) have been unwrapped, the system can be solved by least squares in a process called ‘temporal adjustment’ (Beauducel *et al.* 2000; Feigl *et al.* 2000). In general, however, the problem requires some constraints to regularize the solution because the differencing operator \mathbf{D} is rank deficient. Specifically, the rank deficiency is equal to the number of ‘species’ in the interferometric data set, where we define a species as the set of single-epoch images that can be combined pairwise to form a useful interferogram. According to this definition, any member of a species can form a useful interferometric pair with any other member of the species, either by direct calculation, or by construction, that is, linear combination of pairs of other members of the species. Conversely, members of different species do not form valid interferometric pairs included on the left-hand side of the system of equations described by (2). For example, the data set analyzed here and shown in Fig. 1 contains only a single species. Some images do not form useful interferometric pairs because of temporal decorrelation, orbital separation, or frequency differences. In Fig. 2, the $c = 2$ line segments represent pairs connecting the $q = 3$ epochs, forming an incidence graph (Strang & Borre 1997). Since the path connecting all the epochs does not form a closed loop, we see that the data set does not include any redundant pairs. Topologically, the incidence graph reduces to a tree, according to a formula attributed to Euler (Strang & Borre 1997)

$$\begin{aligned} \text{nodes} - \text{edges} + \text{loops} &= 1 \\ q - c + 0 &= 1 \\ 3 - 2 + 0 &= 1 \end{aligned} \quad (23)$$

To resolve the rank deficiency, the simplest procedure is to set the phase value $\phi^k(t_{j=1})$ at the first epoch in each species to zero. A clever alternative is to rewrite the model parameters in terms of differential phase rate over successive intervals and then find the parameter vector with minimum length by singular value decomposition (Berardino *et al.* 2002). We emphasize, however, that the three previous approaches to linear temporal adjustment (Beauducel *et al.* 2000; Feigl *et al.* 2000; Berardino *et al.* 2002) require unwrapped phase values on the left-hand side of the system of equations described by (2).

When the phase values are wrapped, however, the inverse problem becomes non-linear. We solve the non-linear inverse problem using a simulated annealing algorithm (Kirkpatrick *et al.* 1983) as implemented by Cervelli *et al.* (2001). The procedure is similar to that employed in some previous studies (e.g. Pedersen *et al.* 2003), except that we minimize the cost function $\bar{\omega}$ calculated from wrapped phase values rather than a chi-square measure of misfit calculated from the unwrapped phase values. The simulated annealing algorithm is an effective method to find the “valley” containing the global minimum in the multidimensional misfit space. The algorithm initially samples the model parameter space randomly and then progresses to search more thoroughly near recognized minima.

The randomness in the search permits the algorithm to escape local minima (Cervelli *et al.* 2001; Pedersen *et al.* 2003).

4.3 Statistics of wrapped phase

The wrapped phase residuals θ_i are compatible with a von Mises distribution (Huber *et al.* 2001). To verify this claim, we follow previous work deriving a statistical test (Cox 1975; Barndorff-Nielsen & Cox 1979, 1989, pp. 227–228; Mardia & Jupp 2000, pp. 142–143). In particular, Professor Peter Jupp (personal communication, 2008) has derived the correct expressions in (24)–(26). The test statistic is

$$S_M = \frac{s_c^2}{nv_c(\hat{\kappa})} + \frac{s_s^2}{nv_s(\hat{\kappa})}. \quad (24)$$

where $\hat{\kappa}$ is the maximum-likelihood estimate (Mardia & Jupp 2000) of the concentration parameter κ for the wrapped phase residuals θ_i . This test statistic can be thought of as the ‘sum of squares’ (Cox 1975) of two ratios. The expressions in the numerators of the ratios are

$$\begin{aligned} s_c &= \sum_{i=1}^n \{\cos[2(\theta_i - \bar{\theta})]\} - nI_2(\hat{\kappa})/I_0(\hat{\kappa}) \\ s_s &= \sum_{i=1}^n \{\sin[2(\theta_i - \bar{\theta})]\}, \end{aligned} \quad (25)$$

where $\bar{\theta}$ denotes the mean direction of the wrapped phase residuals and $I_b(\hat{\kappa})$ denotes the modified Bessel function of the first kind and order b evaluated at $\hat{\kappa}$. The expressions in the denominators of the ratios are

$$\begin{aligned} v_c &= \frac{I_0^2 + I_0I_4 - 2I_2^2}{2I_0^2} - \frac{(I_0I_3 + I_0I_1 - 2I_1I_2)^2}{2I_0^2(I_0^2 + I_0I_2 - 2I_1^2)} \\ v_s &= \frac{(I_0 - I_4)(I_0 - I_2) - (I_1 - I_3)^2}{2I_0(I_0 - I_2)}. \end{aligned} \quad (26)$$

For large samples, the test statistic S_M is approximately distributed as a chi-squared distribution with two degrees of freedom. The null hypothesis states that the sample is compatible with a von Mises distribution. The null hypothesis should be rejected for large values of S_M (Mardia & Jupp 2000). For example, we consider a sample of 10^4 random deviates drawn from a von Mises distribution using the RANDRAW routine (Bar-Guy & Podgaetsky 2005). Ten such drawings yield values for the test statistic S_M that range from 0.2 to 4.8. Since all these values are less than the critical value of $\chi_2^2 \doteq 5.99$ at the 0.05 significance level, the null hypothesis fails to be rejected. Accordingly, we conclude that the deviates are compatible with a von Mises distribution, as expected. We apply this test to the phase residuals for the FawnSkin case in Section 5 below.

Assuming that the phase residuals are compatible with a von Mises distribution, we can compare how well different estimates of the model parameters fit the phase data. To do so, we perform a two-sample test to test the null hypothesis that the concentration parameters of two sets of residuals are equal (Mardia & Jupp 2000). This test involves calculating the mean resultant lengths \bar{R}_1 and \bar{R}_2 for each set of residuals. We use the test statistic of Mardia & Jupp (2000, p. 133). For clarity, we denote this two-sample test statistic v_2 . It is approximately distributed as a standard normal $Z \sim N(0, 1)$ with zero mean and unit variance. We apply this statistical test to the FawnSkin interferograms in two ways. First, we use it to compare the final estimate to the initial estimate. Then we use it to determine the uncertainties of the final estimate of the model parameters.

Table 1. Estimated parameters. Parameters in the simulated annealing step of GIPhT, including the initial estimate, the final estimate, the adjustment (final less initial), the uncertainty (sigma), the significance ratio (adjustment divided by uncertainty), the lower bound and the upper bound.

Parameter and units	Initial	Final	Adjust	Sigma	Ratio	Lower	Upper
E grad @ epoch 01 (mm m ⁻¹)	-2.05E-03	-2.63E-03	-5.80E-04	5.10E-04	1.14	-3.00E-03	-1.00E-03
E grad @ epoch 02 in (mm m ⁻¹)	0	0	0	0		0	0
E grad @ epoch 03 (mm m ⁻¹)	0	0	0	0		0	0
N grad @ epoch 01 (mm m ⁻¹)	-5.48E-03	-5.31E-03	1.74E-04	6.05E-04	0.29	-5.50E-03	-4.50E-03
N grad @ epoch 02 (mm m ⁻¹)	0	0	0	0		0	0
N grad @ epoch 03 (mm m ⁻¹)	0	0	0	0		0	0
U grad @ epoch 01 (mm m ⁻¹)	0	0	0	0		0	0
U grad @ epoch 02 (mm m ⁻¹)	0	0	0	0		0	0
U grad @ epoch 03 (mm m ⁻¹)	0	0	0	0		0	0
Offset @ epoch 01 (mm)	0	0	0	0		0	0
Offset @ epoch 02 (mm)	1.00E+01	-9.24E+00	-1.92E+01	2.10E+00	9.16	-1.40E+01	1.40E+01
Offset @ epoch 03 (mm)	1.00E+01	-8.64E+00	-1.86E+01	1.82E+00	10.24	-1.40E+01	1.40E+01
Okada length (m)	2.34E+03	2.26E+03	-7.96E+01	1.33E+02	0.60	2.00E+03	2.86E+03
Okada width (m)	2.78E+03	3.02E+03	2.40E+02	2.40E+02	1.00	2.61E+03	3.10E+03
Okada depth (m)	2.00E+03	1.69E+03	-3.07E+02	1.50E+02	2.05	1.00E+03	3.00E+03
Okada Negative dip (°)	-5.00E+01	-3.91E+01	1.09E+01	3.38E+00	3.23	-6.00E+01	-3.50E+01
Okada strike CW from N (°)	2.83E+02	2.82E+02	-1.21E+00	7.35E+00	0.16	2.70E+02	3.00E+02
Okada easting (m)	0	3.79E+02	3.79E+02	1.10E+02	3.44	-5.00E+02	5.00E+02
Okada northing (m)	2.00E+03	1.07E+03	-9.25E+02	9.75E+01	9.49	1.00E+03	2.50E+03
Okada LL strike slip (m)	-1.99E-02	-2.34E-02	-3.55E-03	3.45E-02	0.10	-5.00E-02	-1.00E-02
Okada downdip slip (m)	-5.63E-01	-5.34E-01	2.85E-02	3.00E-02	0.95	-1.00E+00	0
Okada tensile opening (m)	0	0	0	0		0	0
Constant offset (mm)	0	0	0	0		0	0

5 RESULTS

We apply our technique, GIPhT, to maps of the difference in phase between two SAR images of the FawnSkin epicentral area acquired at different times (Figs. 2a and 3a). In time, the data set consists of $q = 3$ epochs that form $c = 2$ pairs. The first epoch t_1 is common to both pairs. For the time function, we use the Heaviside step function $f(t) = H(t_s)$ that switches from 0 to 1 at the epoch $t_s = 1992.9$ of the FawnSkin aftershock, 1992 December 4. In this case, the time function is ‘off’, $f(t) = 0$, for the first pair (Fig. 2) and is ‘on’, $f(t) = 1$, for the second pair (Fig. 3).

In space, the study area consists of an approximately 8 km \times 8 km rectangle containing 9600 pixels, each of which is 3 seconds of latitude by 3 seconds of longitude, as described previously (Feigl *et al.* 1995). To reduce the volume of data, decrease the computation time, and mitigate the effect of correlated pixels, we randomly select 1 pixel in 32 for a total of $n_r = 300$ pixels. Thus the data set consists of $n = cn_r = 600$ wrapped phase values. The differencing matrix $\mathbf{D}^k = \mathbf{D}$ is the same at all locations, such that it does not depend on the pixel index k . For the mapping function $g(\mathbf{X})$, we use an elastic dislocation formulation (Okada 1985) with nine free parameters: easting, northing, depth, length, width, strike, dip, left-lateral slip and downdip slip. The unit vector $\hat{\mathbf{s}}^{(k)}$ is calculated at each pixel using the orbital trajectory for the first epoch $t_1 = 1992.3$ that is in common to both pairs.

For the nuisance function h^k , we estimate the two horizontal components $h_E(t_1)$ and $h_N(t_1)$ of the phase gradient at the first epoch. These two parameters account for parallel fringes such as those visible in the first interferogram (Fig. 2a). In our case, these fringes are caused by the Landers main shock outside the study area. In most cases, however, such fringes are produced by errors in the satellite’s orbital trajectory. In addition, we estimate nuisance parameters $h_0(t_2)$ and $h_0(t_3)$ at the second and third epochs to account for additional atmospheric and orbital effects. Thus we estimate 9

parameters for the Okada source and 4 nuisance parameters for a total of 13 free parameters.

The initial estimate $\mathbf{m}^{\text{initial}}$ is a reasonable ‘first guess’, based on intentionally degrading the solution determined in the previous study (Feigl *et al.* 1995). We have changed the value of the depth parameter in the initial estimate from 2.8 to 2.0 km (reckoned to the top of the rupture patch). It leads to the simulated fringe patterns shown in Figs. 2b and 3b, as well as the initial residual fringe patterns shown in Figs. 2c and 3c. This initial set of parameter values has a cost of $\bar{\omega}(\mathbf{m}^{\text{initial}}) = 0.2796$. The simulated annealing algorithm searches the parameter space by evaluating the cost of many different trial estimates $\mathbf{m}^{\text{trial}}$. The search is constrained by placing bounds $\mathbf{m}^{\text{lower}} \leq \mathbf{m}^{\text{trial}} \leq \mathbf{m}^{\text{upper}}$ as listed in Table 1. Upon convergence at the presumed global minimum in cost $\bar{\omega}(\mathbf{m}^{\text{final}}) = 0.1483$, the simulated annealing algorithm gives the final estimate $\mathbf{m}^{\text{final}}$ of the model parameters listed in Table 1. This final estimate produces the simulated fringe patterns shown in Figs. 2f and 3f, the final residual fringe patterns shown in Figs. 2g and 3g, and the final angular deviations shown in Figs. 2h and 3h. Histograms of the initial and final wrapped phase residuals are shown in Fig. 5. To evaluate the quality of this solution, we perform several statistical tests on the wrapped phase residuals.

5.1 Statistical analysis of the phase residuals

First, we verify that the wrapped phase residuals θ are compatible with a von Mises distribution. For the residuals calculated from the final estimate of the model parameters, the test statistic described above takes the value $S_M \doteq 2.06$. Since this value is less than the critical value of $\chi^2_2 \doteq 5.99$ at the 0.05 significance level, the null hypothesis is not rejected ($P \doteq 0.35$). Accordingly, we conclude that the final phase residuals θ_i are compatible with a von Mises distribution.

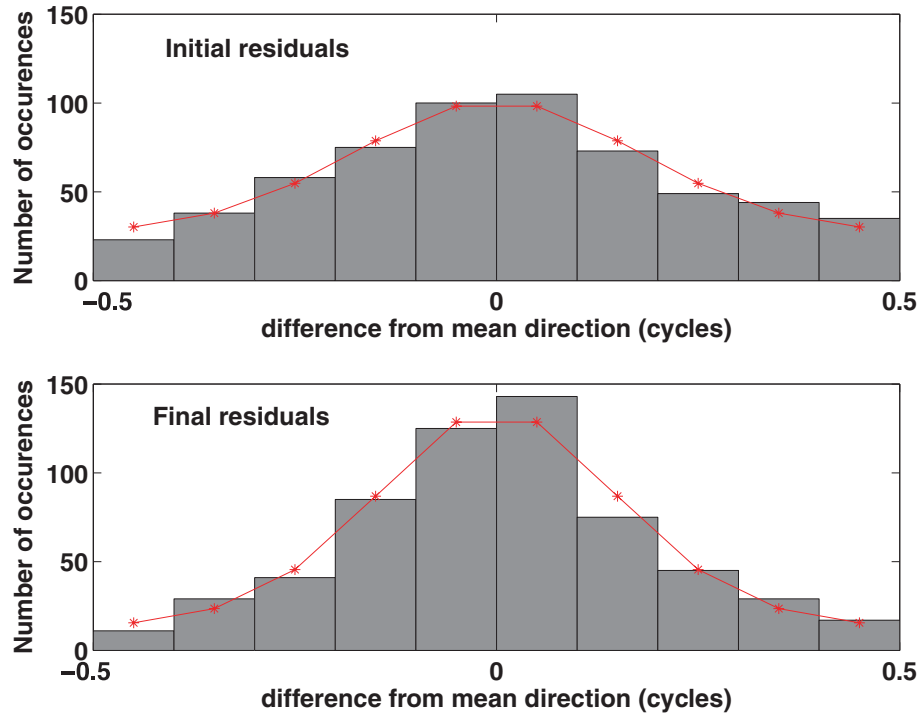


Figure 5. Histogram of the wrapped phase residuals θ_i in cycles for the initial estimate (above) and final estimate (below). The curves indicate the number of occurrences expected from von Mises distributions with a mean direction $\bar{\theta} = 0$, sample size $n = 600$ and concentration parameters $\hat{\kappa} = 0.63$ for the initial residuals; $\hat{\kappa} = 1.13$ for the final residuals.

Alternatively, we can calculate the cumulative frequency values of the residuals and compare them to the cumulative frequency values expected from a von Mises distribution. Plotting the former as a function of the latter yields the quantile–quantile (Q - Q) plot shown in Fig. 6. The points fall on a line with unit slope, indicating that the final wrapped phase residuals are compatible with a von Mises distribution.

To test this inference formally, we sort the cumulative frequency values $z_i = F_{\hat{\kappa}}(\theta_i - \bar{\theta})$ calculated using the cumulative von Mises distribution $F_{\hat{\kappa}}$ into increasing order and compute the statistic (Fisher 1993, p. 84, as corrected in the first paperback edition)

$$U^2 = \sum_{i=1}^n \left(z_i - \frac{2i-1}{2n} \right)^2 - n \left(\bar{z} - \frac{1}{2} \right)^2 + \frac{1}{12n}. \quad (27)$$

The null hypothesis is that the final wrapped phase residuals have been drawn from a von Mises distribution. It is not rejected because the value of the test statistic $U^2 \doteq 0.05$ is smaller than the critical value of 0.09 at the 0.05 significance level with mean direction unknown and concentration parameter unknown (Fisher 1993, Table A8, p. 230). Accordingly, we again infer that the phase residuals θ_i are compatible with a von Mises distribution.

The mean direction of the wrapped residuals from the final estimate is $\bar{\theta}(\mathbf{m}^{\text{final}}) \doteq -0.01$ cycles. We test the null hypothesis that the corresponding parameter equals zero using eq. (4.56) of Fisher (1993, pp. 93–94). Since the null hypothesis fails to be rejected ($P \doteq 0.39$), we infer that the mean direction of the final residuals is not significantly different from zero.

The circular standard deviation of the final wrapped phase residuals is $v = \sqrt{-2 \log \bar{R}} \doteq 0.2$ cycle (eq. 2.3.11 of Mardia & Jupp 2000, p. 19). This phase value corresponds to 6 mm in range, com-

parable to the 7 mm root mean square scatter in the unwrapped range residuals found in the previous study (Feigl *et al.* 1995).

Fig. 5 shows that the final phase residuals are more concentrated than the initial residuals, confirming that the final estimate $\mathbf{m}^{\text{final}}$ of the parameters fits the data better than the initial estimate $\mathbf{m}^{\text{initial}}$. The mean resultant lengths for residuals from the initial and final estimates are $\bar{R}(\mathbf{m}^{\text{initial}}) = 0.3005$ and $\bar{R}(\mathbf{m}^{\text{final}}) = 0.4906$, respectively. We use the two-sample statistic v_2 (Mardia & Jupp 2000, p. 133) to test the null hypothesis that the von Mises concentration parameters of residuals from the initial and final estimates are equal $\kappa(\mathbf{m}^{\text{initial}}) = \kappa(\mathbf{m}^{\text{final}})$. Since the two-sample statistic $v_2 \doteq -5.34$ is less than the two-tailed critical value $Z_{0.025} \doteq -1.96$ for the standard normal distribution at the 0.05 significance level, we reject the null hypothesis ($P < 10^{-6}$). Thus the initial and final residuals are concentrated differently. We conclude that the final estimate fits the data significantly better than does the initial estimate.

5.2 Uncertainties of the estimated model parameters

To evaluate the uncertainty of the parameter estimates, we vary each model parameter m_l independently and calculate the average cost $\bar{\omega}(m_l)$, holding fixed the other elements of the model parameter vector \mathbf{m} . Fig. 7 shows this calculation for the width parameter in the fault model.

The one-sigma uncertainty of the estimated parameter is approximately the half-width of the ‘valley’ of average cost measured at a ‘height’ $\bar{\omega}(\mathbf{m}_{69\%})$ corresponding to the interval of 69 per cent confidence. To find this value, we test the null hypothesis that the concentration parameters of two sets of residuals are equal (Mardia & Jupp 2000). This test involves calculating the mean resultant lengths \bar{R}_1 and \bar{R}_2 for each set of residuals. Since $0.45 \leq \bar{R} \leq 0.70$, we use

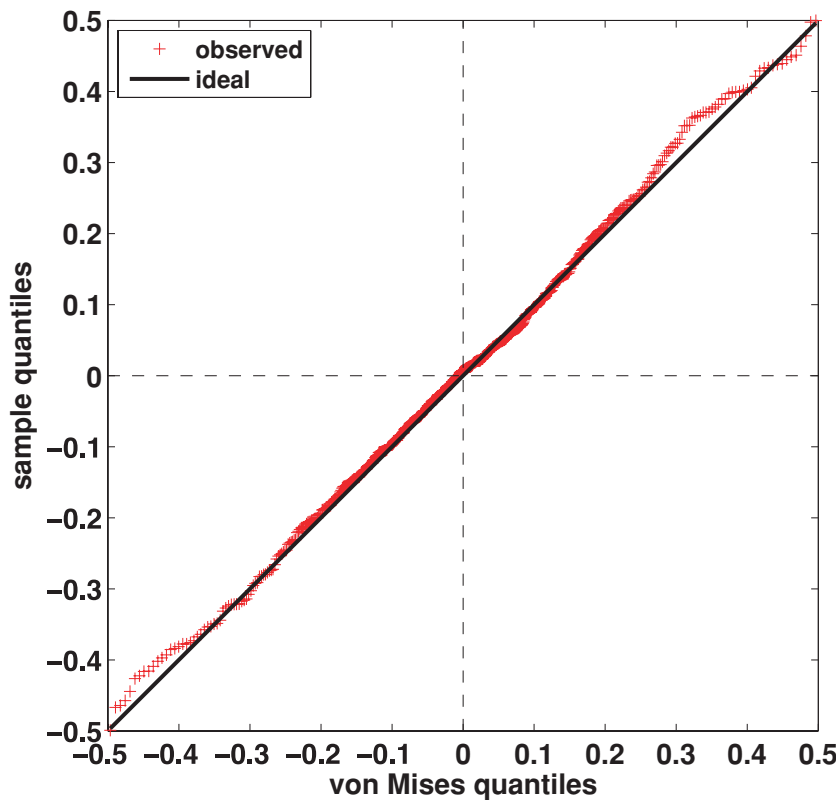


Figure 6. Quantile–quantile (Q – Q) plot of the final wrapped phase residuals showing that they are compatible with a von Mises distribution. The vertical axis shows the quantiles for the final phase residuals $\theta_i^{(\text{final})}$ in wrapped cycles. The horizontal axis shows the quantiles expected for von Mises distribution with a mean direction $\bar{\theta} = 0$, a concentration parameter $\hat{k} = 1.13$, and a sample size $n = 600$.

case II of the two-sample test statistic v_2 given by eq. (7.3.24) of Mardia & Jupp (2000, p. 133). The test statistic v_2 is approximately distributed as a standard normal $Z \sim N(0, 1)$ with zero mean and unit variance. We set $Z = -0.48$ for a single-tailed critical region with 69 per cent confidence. The mean resultant length is $\bar{R}_2 = 0.4906$ for the residuals from the final estimate of the model parameters (sample 2). We find that the mean resultant length for the residuals from the trial estimates (sample 1) must reach $\bar{R}_1 = 0.4742$ to reject the null hypothesis for $n_1 = n_2 = 600$ data. The critical value of the average cost is thus $\bar{\omega}(\mathbf{m}_{69\%}) = 0.1531$, using an empirical relationship developed with a random number generator (Bar-Guy & Podgaetsky 2005). This critical value appears as a horizontal dashed line in Fig. 7. Its intersections with the curve of average cost values determine the width of the one-sigma ‘error bar’ for the parameter. In the case where one of these intersections falls outside the bounds constraining the simulated annealing search, the confidence interval ends at the input constraint.

5.3 Robustness of the estimated model parameters

To evaluate how well GIPhT converges, we perform a Monte Carlo analysis of 100 runs. The lower and upper bounds are listed in Table 1, as before. In each run, however, we randomly select the $n_r = 600$ pixels anew. The simulated annealing algorithm finds a final estimate with a lower cost than for the initial estimate in 81 of the 100 runs. In these 81 solutions, the root mean square scatter of the final estimate of the depth parameter is 280 m. The algorithm finds a final cost lower than 0.1600 in 40 of the 100 runs. For these 40 runs, the mean uncertainty of the final depth estimate is

176 m and the root mean scatter of the final depth estimates is 88 m. These results indicate that the uncertainty of ± 150 m in the final depth estimate of the solution listed in Table 1 accounts adequately for the noise in the phase data. These results indicate that the uncertainty of the depth parameter estimated here is better than the ± 300 m uncertainty determined in the previous study (Feigl *et al.* 1995). Presumably, the uncertainties for the other estimated parameters listed in Table 1 are also valid because they are calculated in the same manner.

6 DISCUSSION

The final estimate of the model parameters fits the observed interferograms better than the initial estimate. For example, the concentric pattern in the final model (Fig. 3f) more closely resembles the observation (Fig. 3a) than does the pattern in the initial model (Fig. 3b). The initial residual interferogram (Fig. 3c) shows over two fringes (>56 mm in range change) in a pattern with two lobes, while the final residual interferogram (Fig. 3g) shows no spatially coherent structure. Similarly, the final angular deviations (Fig. 3h) are smaller than the initial deviations (Fig. 3d).

To illustrate that the model fits the data, Fig. 8 shows the range change in profile. The range change calculated from the final estimate of the model parameters agrees with the unwrapped measurements to within their uncertainties. Here we have assigned the uncertainty for one measurement to equal the circular standard deviation of the final wrapped phase residuals (0.2 cycle) multiplied by the half-wavelength of 28 mm. Several caveats apply to Fig. 8, however. The circles show the observed phase value after

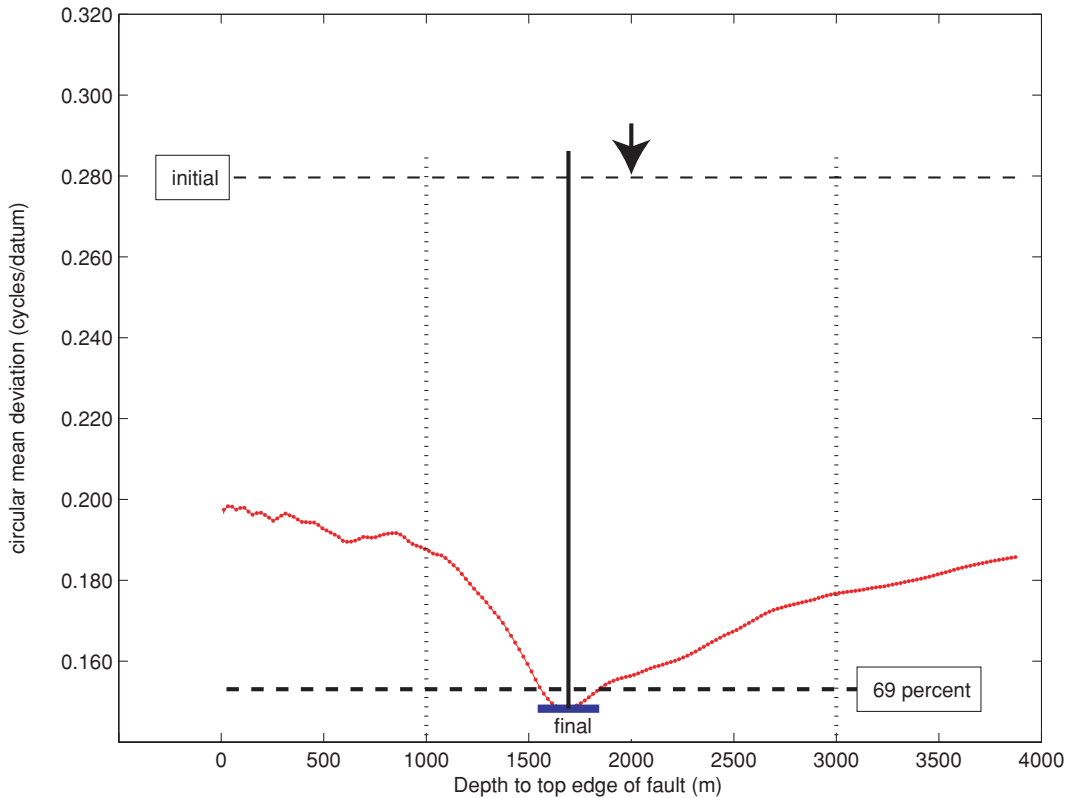


Figure 7. Cross-section through the parameter space showing how GIPhT evaluates the uncertainty of an estimated parameter, as described in Section 5.2 of the text. The cost $\bar{\omega}$ is plotted as a function of the parameter describing the depth to the upper edge of the rectangular rupture zone that slipped during the FawnSkin aftershock. Horizontal dashed lines indicate: the value of cost for the initial estimate of the model parameters, the critical value of cost $\bar{\omega}(m_{69\%})$ at 69 per cent confidence, and the value of cost for the final estimate of the model parameters, respectively, from top to bottom. Vertical lines indicate the parameter values for the final estimate of the model parameters (solid line), the initial estimate (short arrow), as well as the lower and upper bounds constraining the simulated annealing search (dotted lines). The short horizontal bar indicates the 1σ (69 per cent) confidence interval for the estimated depth parameter.

unwrapping in two different ways. The filled circles show the values obtained by adding the (unwrapped) final modelled values and the (wrapped) final residual values $\Delta\phi = \Delta\tilde{\phi} + \theta$. By construction, however, the filled circles must fall within $\pm\frac{1}{2}$ cycle in phase, that is, ± 14 mm in range, of the model curve. In other words, the unwrapped phase values depend on the model. The phase values unwrapped in this way are convenient for illustration. They should not, however, be used in further quantitative analysis because using GIPhT for unwrapping in this way might incur all the drawbacks it was designed to avoid. The open circles in Fig. 8 show the range change after applying a simple 1-D routine to unwrap the observed phase values without any model. The departure of the open circles from the model curve between 34.34°N and 34.35°N is of the order of 28 mm in range or 1 cycle in phase, which we interpret as an indication of an unwrapping error. If these data had been used in a least-squares inversion, the estimated parameters would be in error.

Table 2 compares the final estimate to several other solutions. The final estimate determined by applying GIPhT to wrapped phase data does not differ significantly from the previous estimate determined by applying iterative least squares to unwrapped phase data in the previous study (Feigl *et al.* 1995), as the differences between the estimates do not exceed their combined uncertainties. For example, the previous study estimates the thrust component of slip to be 514 ± 37 mm, in good agreement with the value of 534 ± 30 mm estimated here. To compare the goodness of fit for the two approaches, we use the result from the previous study as the initial estimate in GIPhT, applying tight constraints

on the geophysical parameters in the mapping function g^k and loose constraints on the parameters in the nuisance functions h^k . Since the two-sample statistic $v_2 \doteq -0.47$ falls between the two critical values for the standard normal distribution, we do not reject the null hypothesis that the two samples of wrapped phase residuals are equally concentrated ($P \doteq 0.32$). Thus we conclude that the phase values analysed in the previous study were correctly unwrapped.

In the final estimate, the rupture plane dips $38^\circ \pm 4^\circ$ to the south. If we instead set the initial estimate to a north-dipping plane, GIPhT finds another solution that dips $35^\circ \pm 3^\circ$ to the north with a cost of $\bar{\omega} \doteq 0.1516$ cycle per datum. Although this value is greater than that for the south-dipping solution with a cost of $\bar{\omega} \doteq 0.1483$ cycle per datum, the difference is not significant. Since the value of the two-sample statistic $v_2 \doteq 0.16$ falls between the two critical values for the standard normal distribution, we do not reject the null hypothesis that the two samples of wrapped phase residuals are equally concentrated ($P \doteq 0.40$). As discussed in the previous study, the south-dipping solution is consistent with the southward dip of the North Frontal fault and Sky Hi Ranch fault which bound the San Bernardino Mountains by dipping below them (Meisling & Weldon 1989). Furthermore, most of the small aftershocks occur south of the surface traces of these faults (Hauksson *et al.* 1993), as shown in Fig. 1 of the previous study (Feigl *et al.* 1995). Therefore, we prefer the south-dipping solution.

As in the previous study, the uncertainties of the parameter estimates are formal in the sense that they do not account for systematic

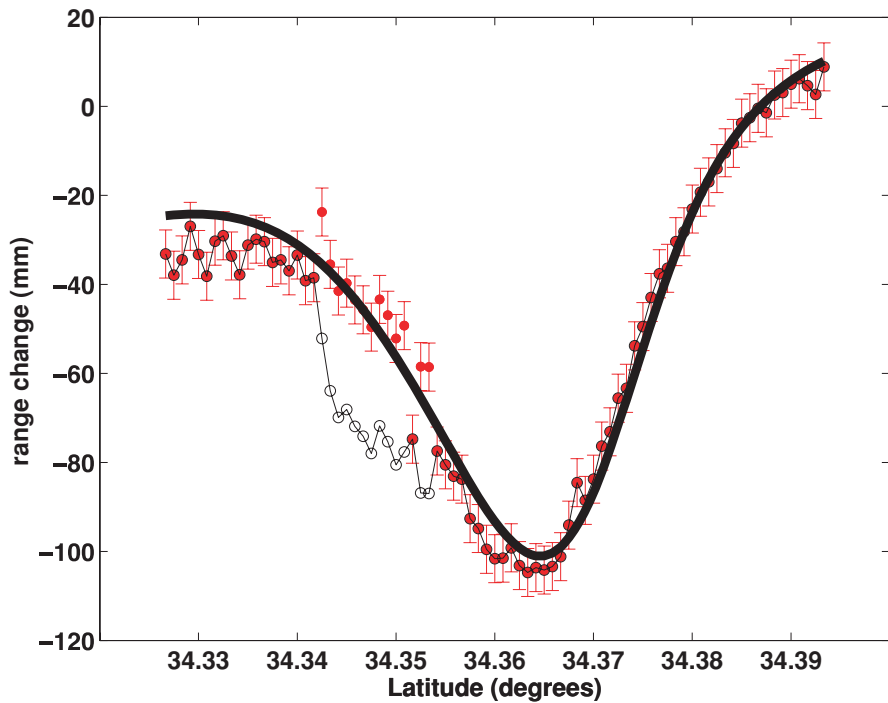


Figure 8. Profile of range change showing the agreement between model and data. The profile follows a north–south line through the centre of the top edge of the rupture surface as determined from the final estimate. The thick curve shows the modelled value of range change calculated from the final estimate. The circles show the observed range change calculated by multiplying the unwrapped observed phase value by 28 mm cycle^{-1} . The phase values have been unwrapped in two different ways. The filled circles show the values obtained by adding the final modelled values to the final residual values. The error bars are $\pm 6 \text{ mm}$ in range, calculated from the 0.2-cycle circular standard deviation of the final phase residuals. By construction, the filled circles must fall within $\pm \frac{1}{2}$ cycle of the model curve. The open circles show the observed range after applying a simple 1-D routine to unwrap the observed phase values without a model. The departure of the open circles from the model curve between 34.34°N and 34.35°N is indicative of an unwrapping error.

Table 2. Focal mechanism parameters for FawnSkin aftershock at 02:08 GMT on 1992 December 4. Comparison of earthquake source parameters for the FawnSkin aftershock estimated by various studies. The latitude, longitude and depth refer to the centre of a rectangular patch of slip. Strike (str), dip, and rake (rak) follow the convention of Aki & Richards (1980). The U_1 and U_2 components of slip are reckoned positive for left-lateral and up-dip slip, respectively, as defined by Okada (1985).

Study	Lat (°)	Lon (°)	Depth (km)	str (°)	dip (°)	rak (°)	U_1 (mm)	U_2 (mm)	U_3 (mm)	L (km)	W (km)	M_w	Cost (cycle datum $^{-1}$)
Estimates													
Hauksson <i>et al.</i> (1993)	W116.90	N34.37	1.8	95	55	120							5.1
Jones & Hough (1994)	W116.90	N34.35	7	126	43	117							5.1
Feigl <i>et al.</i> (1995)	W116.91	N34.35	2.6	106	28	93	-22	514	0	2.9	3.1	5.1	0.1775
This study (S-dipping)	W116.91	N34.36	2.7	102	39	92	-23	534	0	2.3	3.0	5.3	0.1483
This study (N-dipping)	W116.91	N34.37	2.5	263	31	92	-22	566	0	2.4	2.7	5.3	0.1516
Uncertainties													
Hauksson <i>et al.</i> (1993)	1	1	1	10	24	25							
Feigl <i>et al.</i> (1995)	0.2	0.4	0.3	7	4	4	40	37		0.4	0.5		0.1
This study (S-dipping)	1.0	0.11	0.15	7	4		35	30		0.13	0.24		
This study (N-dipping)	0.09	0.11	0.13	7	2		2	3		0.13	0.14		

Notes: Position coordinates are for centre of rectangular slip patch. M_w magnitude assumes a shear modulus of 30 GPa.

errors in the measurements, correlations in the data, or oversimplifications in the physical earth model. For example, we assume the phase data to be independent in all our statistical tests. Although neighbouring pixels are correlated in space (Hanssen 2001; Lohman & Simons 2005b) and pairs sharing a common epoch are correlated in time (Biggs *et al.* 2007), the parameter estimates are robust to different (randomly selected) subsets of the pixels, as discussed in Section 5.3 above. The scatter in the depth estimates is comparable to the uncertainty of $\pm 150 \text{ m}$ found by GIPhT for the final estimate (Table 1). We conclude that the procedure of randomly

selecting pixels mitigates the issue of correlation. Fully accounting for spatial and temporal correlations in wrapped phase data would involve statistical derivations using the von Mises distribution that are beyond the scope of this paper.

7 CONCLUSION

We have developed, validated and applied GIPhT for modelling the phase changes recorded by InSAR. By minimizing a cost function defined in terms of wrapped phase, GIPhT can estimate the

parameters in a non-linear model. GIPhT offers the following advantages. (1) GIPhT can identify species of pairs within set of interferograms to select a data set with no redundant pairs. (2) GIPhT can handle several species of interferometric pairs, even in the case where no single epoch partakes in all pairs. (3) GIPhT applies to any InSAR data set that can be described by a model that separates the temporal dependence from the spatial dependence. (4) Since the wrapped phase residuals are compatible with a von Mises distribution, standard parametric statistical tests can be used to evaluate the fit of the model to the data. The same parametric statistical tests also enable GIPhT to determine the uncertainties of the estimated model parameters. (5) GIPhT avoids the potential drawbacks of phase-unwrapping approaches by working directly with wrapped phase. Thus GIPhT can be used to analyse interferograms with poor interferometric correlation. If reliable pixels can be selected by their amplitude dispersion (e.g. Ferretti *et al.* 2001; Lyons & Sandwell 2003; Akarvardar *et al.* 2007), then their phase values can be modelled by GIPhT even if the areal density of the selected pixels is too sparse to permit unwrapping. (6) The modelled phase values calculated from the final estimate of the parameters can be used to calculate an unwrapped version of the observed phase values. The validity of this calculation, however, depends on the validity of the estimated model parameters.

Applying GIPhT to two interferograms in the San Bernardino Mountains, we have estimated a set of model parameters, including the source parameters of the Fawnksin aftershock of 1992 December 4. Since the slip in this earthquake does not reach the Earth's surface, there is no need to estimate the differential range change between the two blocks separated by the fault. For an earthquake with such surface rupture, however, GIPhT could estimate the slip at the surface as an offset in phase. Resolving the integer part of this parameter, however, would require coherent fringes connecting the two blocks or independent information from, say, surveys using the Global Positioning System (GPS). In this situation, whether one uses wrapped or unwrapped data in the inverse modelling, the results are likely to be similar.

As a result of the GIPhT analysis of the Fawnksin earthquake, we reach the following conclusions. (1) The resulting simulation fits the measurements to within 0.2 cycles in phase or 6 mm in range. (2) The GIPhT estimate of the focal mechanism using wrapped phase data is not significantly different from a previous estimate using unwrapped phase data. (3) GIPhT finds two acceptable geometric configurations for the predominantly thrust focal mechanism: one with a south-dipping fault plane and a second with a north-dipping fault plane. The south-dipping fault plane solution is consistent with the mapped faults and seismicity. Although the solution with a south-dipping fault plane has a lower cost than the north-dipping solution, the difference is not significant. (4) The uncertainties of the estimated parameters are small. For example, the centroid location for Fawnksin aftershock is precise to within 300 m in all three components of position. The estimate of the angles in the focal mechanism are precise to within 10° for strike, dip and rake. The length and width of the fault patch are precise to within 1 km.

The precision in the parameters estimated by GIPhT comes from the capability of InSAR to measure coseismic deformation with centimetre-level precision at pixels located within a few kilometres of the earthquake source, as demonstrated for several shallow earthquakes of moderate magnitude (e.g. Feigl *et al.* 1995; Pedersen *et al.* 2001; Lohman *et al.* 2002; Pedersen *et al.* 2003; Lohman & Simons 2005a; Mellors *et al.* 2004). Accordingly, it seems worthwhile to apply GIPhT to other examples of present-day deformation.

ACKNOWLEDGEMENTS

We gratefully thank Didier Massonnet for pointing out the geometric interpretation of summing the residual phasors. We are indebted to Peter Jupp for his patient tutoring with an invaluable textbook. We also thank Sebastian Chevrot, Samuray Akarvardar, Lee Powell and Zhong Lu for interesting discussions. Two anonymous reviewers provided helpful comments.

REFERENCES

- Akarvardar, S., Feigl, K.L. & Ergintav, S., 2007. Subsidence in the Avcılar district of Istanbul, Turkey measured by satellite radar interferometry 1992–1999, *Geophys. J. Int.*, in revision.
- Aki, K. & Richards, P.G., 1980. Quantitative Seismology, 932 pp., W.H. Freeman, New York.
- Bar-Guy, A. & Podgaetsky, A., 2005. RANDRAW: an efficient random variates generator, v. 1, Matlab File Exchange.
- Barndorff-Nielsen, O. & Cox, D.R., 1979. Edgeworth and saddle-point approximations with statistical applications, *J. R. Stat. Soc. Ser. B (Methodological)*, **41**, 279–312.
- Barndorff-Nielsen, O.E. & Cox, D.R., 1989. *Asymptotic Techniques for Use in Statistics*, Chapman and Hall, New York.
- Beauducel, F., Briole, P. & Froger, J.L., 2000. Volcano wide fringes in ERS synthetic aperture radar interferograms of Etna: deformation or tropospheric effect?, *J. Geophys. Res.*, **105**, 16 391–16 402.
- Berardino, P., Fornaro, G., Lanari, R. & Sansosti, E., 2002. A new algorithm for surface deformation monitoring based on small baseline differential SAR interferograms, *IEEE Trans. Geosci. Remote Sens.*, **40**, 2375.
- Biggs, J., Bergman, E., Emmerson, B., Funning, G.J., Jackson, J., Parsons, B. & Wright, T.J., 2006. Fault identification for buried strike-slip earthquakes using InSAR: the 1994 and 2004 Al Hoceima, Morocco earthquakes, *Geophys. J. Int.*, **166**, 1347–1362.
- Biggs, J., T., W., Lu, Z. & Parsons, B., 2007. Multi-interferogram method for measuring interseismic deformation: Denali Fault, Alaska, *Geophys. J. Int.*, **170**, 1165–1179.
- Cervelli, P., Murray, M.H., Segall, P., Aoki, Y. & Kato, T., 2001. Estimating source parameters from deformation data, with an application to the March 1997 earthquake swarm off the Izu Peninsula, Japan, *J. Geophys. Res.*, **106**, 11 217–11 237.
- Chen, C.W. & Zebker, H.A., 2000. Network approaches to two-dimensional phase unwrapping: intractability and two new algorithms, *J. Opt. Soc. Am. A*, **17**, 401–414.
- Chen, C.W. & Zebker, H.A., 2001. Two-dimensional phase unwrapping with use of statistical models for cost functions in nonlinear optimization, *J. Opt. Soc. Am. A*, **18**, 338–351.
- Chen, C.W. & Zebker, H.A., 2002. Phase unwrapping for large SAR interferograms: statistical segmentation and generalized network models, *IEEE Trans. Geosci. Remote Sens.*, **40**, 1709–1719.
- Colesanti, C., Ferretti, A., Novali, F., Prati, C. & Rocca, F., 2003. SAR monitoring of progressive and seasonal ground deformation using the permanent scatterers technique, *IEEE Trans. Geosci. Remote Sens.*, **41**, 1685–1701.
- Cox, D.R., 1975. Contribution to discussion of Mardia (1975a), *J. R. Stat. Soc., Ser. B*, **37**, 380–381.
- Feigl, K.L., 2002. Measurement of coseismic deformation by satellite geodesy, in *International Handbook of Earthquake and Engineering Seismology*, pp. 607–620, eds Lee, W.H.K., Kanamori, H. & Jennings, P.C., Academic Press, London.
- Feigl, K.L. & Thatcher, W., 2006. Geodetic observations of post-seismic transients in the context of the earthquake deformation cycle, *Compt. Rendus – Geosci.*, **338**, 1012–1028.
- Feigl, K.L., Sergent, A. & Jacq, D., 1995. Estimation of an earthquake focal mechanism from a satellite radar interferogram: application to the December 4, 1992 Landers aftershock, *Geophys. Res. Lett.*, **22**, 1037–1048.

- Feigl, K.L., Gasperi, J., Sigmundsson, F. & Rigo, A., 2000. Crustal deformation near Hengill volcano, Iceland 1993–1998: coupling between volcanism and faulting inferred from elastic modeling of satellite radar interferograms, *J. geophys. Res.*, **105**, 26 555–25 670.
- Ferretti, A., Prati, C. & Rocca, F., 2000. Nonlinear subsidence rate estimation using permanent scatterers in differential SAR interferometry, *IEEE Trans. Geosci. Remote Sens.*, **38**, 2202–2212.
- Ferretti, A., Prati, C. & Rocca, F., 2001. Permanent scatterers in SAR interferometry, *IEEE Trans. Geosci. Remote Sens.*, **39**, 8–20.
- Fialko, Y., 2004. Evidence of fluid-filled upper crust from observations of postseismic deformation due to the 1992 Mw 7.3 Landers earthquake, *J. geophys. Res. (Solid Earth)*, **109**, 08401.
- Fisher, N.I., 1993. *Statistical Analysis of Circular Data*, 277 pp., Cambridge University Press, New York.
- Ghiglia, D.C., 1998. *Two-Dimensional Phase Unwrapping: Theory, Algorithms, and Software*, 493 pp. Wiley, New York.
- Ghiglia, D. & Romero, L., 1994. Robust two-dimensional weighted and unweighted phase unwrapping using fast transforms and iterative methods, *J. Opt. Soc. Am. A*, **11**, 107–117.
- Ghiglia, D., Mastin, G. & Romero, L., 1987. Cellular-automata method for phase unwrapping, *J. Opt. Soc. Am. A*, **4**, 267–280.
- Goldstein, R.M., Zebker, H.A. & Werner, C.L., 1988. Satellite radar interferometry: two dimensional phase unwrapping, *Radio Sci.*, **23**, 713–720.
- Hanssen, R.F., 2001. *Radar Interferometry: Data Interpretation and Error Analysis*, 8 pp., Kluwer Academic Publishers, Dordrecht.
- Hauksson, E., Jones, L.M., Hutton, K. & Eberhart-Phillips, D., 1993. The 1992 Landers earthquake sequence, *J. geophys. Res.*, **98**, 19 835–19 858.
- Huber, R., Dutra, L.V. & da Costa Freitas, C., 2001. SAR interferogram phase filtering based on the Von Mises distribution, in *Geoscience and Remote Sensing Symposium, 2001. IGARSS '01. IEEE 2001 International*, pp. 2816–2818, ed. Dutra, L.V. Sydney, Australia, IEEE Operations Center, Piscataway, New Jersey.
- Jones, L.E. & Hough, S.E., 1994. Analysis of broadband recordings of the 6/28/92 Big Bear earthquake: evidence for a multiple-source event, *Bull. Seism. Soc. Amer.*, **88**, 688–704.
- Kirkpatrick, S., Gelatt, C.D., Jr. & Vecchi, M.P., 1983. Optimization by simulated annealing, *Science*, **220**, 671–680.
- Kohlhase, A.O., Feigl, K.L. & Massonnet, D., 2003. Applying differential InSAR to orbital dynamics: a new approach for estimating ERS trajectories, *J. Geod.*, **77**, 493–502.
- Lohman, R.B. & Simons, M., 2005a. Locations of selected small earthquakes in the Zagros mountains, *Geochem., Geophys., Geosyst.*, **6**, Q03001, doi:10.1029/2004GC000849.
- Lohman, R.B. & Simons, M., 2005b. Some thoughts on the use of InSAR data to constrain models of surface deformation: noise structure and data downampling, *Geochem., Geophys., Geosyst.*, **6**, Q01007, doi:10.1029/2004GC000841.
- Lohman, R.B., Simons, M. & Savage, B., 2002. Location and mechanism of the Little Skull Mountain earthquake as constrained by satellite radar interferometry and seismic waveform modeling, *J. geophys. Res.*, **107**, 2118, doi:10.1029/2001JB000627.
- Lyons, S. & Sandwell, D., 2003. Fault creep along the southern San Andreas from interferometric synthetic aperture radar, permanent scatterers, and stacking, *J. geophys. Res.*, **108**, 2047, doi:10.1029/2002JB001831.
- Mardia, K.V., 1972. *Statistics of Directional Data*, 357 pp., Academic Press, New York.
- Mardia, K.V. & Jupp, P.E., 2000. *Directional Statistics*, 429 pp., Wiley, New York.
- Marple, S.L., 1987. *Digital Spectral Analysis with Applications*, 492 pp., Prentice Hall, Englewood cliffs, New Jersey.
- Marroquin, J. & Rivera, M., 1995. Quadratic regularization functionals for phase unwrapping, *J. Opt. Soc. Am. A*, **12**, 2393.
- Massonnet, D., 1997. Reply to ‘Comments on ‘Reduction of the need for phase unwrapping in radar interferometry’’, *Geosc. Remote Sens., IEEE Trans.*, **35**, 1073–1074.
- Massonnet, D. & Feigl, K.L., 1995. Discriminating geophysical phenomena in satellite radar interferograms, *Geophys. Res. Lett.*, **22**, 1537–1540.
- Massonnet, D., Rossi, M., Carmona, C., Adragna, F., Peltzer, G., Feigl, K. & Rabaute, T., 1993. The displacement field of the Landers earthquake mapped by radar interferometry, *Nature*, **364**, 138–142.
- Massonnet, D., Feigl, K.L., Rossi, M. & Adragna, F., 1994. Radar interferometric mapping of deformation in the year after the Landers earthquake, *Nature*, **369**, 227–230.
- MathWorks, 2007. *MATLAB*, v. R2007a, The Mathworks Inc., Natick, Massachusetts.
- Meisling, K.E. & Weldon, R.J., 1989. Late Cenozoic tectonics of the northwestern San Bernardino Mountains, southern California, *Geol. Soc. Am. Bull.*, **101**, 106–128.
- Mellors, R.J., Magistrale, H., Earle, P. & Cogbill, A., 2004. Comparison of moderate earthquake locations in Southern California using seismology and InSAR, *Bull. seism. Soc. Am.*, **94**, 2004–2014.
- Mogi, K., 1958. Relations between the eruption of various volcanoes and the deformations of the ground surfaces around them, *Bull. Earthq. Res. Inst.*, **36**, 99–134.
- Nikolaidis, N. & Pitas, I., 1998. Nonlinear processing and analysis of angular signals, *IEEE Trans. Signal Proc.*, **46**, 3181–3194.
- Okada, Y., 1985. Surface deformation due to shear and tensile faults in a half-space, *Bull. seism. Soc. Am.*, **75**, 1135–1154.
- Pedersen, R., Sigmundsson, F., Feigl, K.L. & Árnadóttir, T., 2001. Coseismic interferograms of two MS = 6.6 earthquakes in the South Iceland Seismic Zone, June 2000, *Geophys. Res. Lett.*, **28**, 3341–3344.
- Pedersen, R., Jónsson, S., Árnadóttir, T., Sigmundsson, F. & Feigl, K.L., 2003. Fault slip distribution of two June 2000 Mw 6.5 earthquakes in South Iceland estimated from joint inversion of InSAR and GPS measurements, *Earth planet. Sci. Lett.*, **213**, 487–502.
- Snyder, J.P., 1982. *Map projections used by the U.S. Geological Survey*, 313 pp., U.S. Gov’t Print. Off., Washington, DC.
- Talebian, M. et al., 2004. The 2003 Bam (Iran) earthquake: rupture of a blind strike-slip fault, *Geophys. Res. Lett.*, **31**, 11611.
- Vadon, H. & Sigmundsson, F., 1997. Crustal deformation from 1992 to 1995 at the mid-Atlantic Ridge, Southwest Iceland, mapped by satellite radar interferometry, *Science*, **275**, 194–197.
- Wright, T.J., Parsons, B.E., Jackson, J.A., Haynes, M., Fielding, E.J., England, P.C. & Clarke, P.J., 1999. Source parameters of the 1 October 1995 Dinar (Turkey) earthquake from SAR interferometry and seismic body-wave modelling, *Earth planet. Sci. Lett.*, **172**, 23–37.
- Wright, T.J., Fielding, E.J., Parsons, B.E. & England, P.C., 2001. Triggered slip: observations of the 17 August 1999 Izmit (Turkey) earthquake using radar interferometry, *Geophys. Res. Lett.*, **28**, 1079–1082.
- Zebker, H.A., Vesecky, J.F. & Lin, Q., 1994. Phase unwrapping through fringe-line detection in synthetic aperture radar interferometry, *Appl. Opt.*, **33**, 201–208.